ORIGINAL ARTICLE

Dissolving microneedles containing aminolevulinic acid improves protoporphyrin IX distribution

Michelle Barreto Requena*,1 | Andi Dian Permana2,3 | Jose Dirceu Vollet-Filho1 | Patricia González-Vázquez2 | Marlon Rodrigues Garcia4, |Clara Maria Gonçalves de Faria1| Sebastião Pratavieira1 |Ryan F. Donnelly2 |Vanderlei Salvador Bagnato1,5

1 São Carlos Institute of Physics, University of São Paulo, São Carlos - SP, Brazil.
2 School of Pharmacy, Queen's University Belfast, Belfast, UK.
3 Department of Pharmaceutics, Faculty of Pharmacy, Hasanuddin University, Makassar, Indonesia.
4 Department of Mechanical Engineering, University of São Paulo, São Carlos - SP, Brazil.
5 Hagler Institute for Advance Studies - Texas A&M University, College Station, USA.

Correspondence
Michelle Barreto Requena, São Carlos Institute of Physics, University of São Paulo, Av. Trabalhador são-carlense, 400, PO Box 369, 13560-970, São Carlos, SP, Brazil.
Email: requenamichelle@gmail.com

One important limitation of topical photodynamic therapy (PDT) is the limited tissue penetration of precursors. Microneedles (MNs) are minimally invasive devices used to promote intradermal drug delivery. Dissolving MNs contain drug-associated to polymer blends, dissolving after insertion into skin, allowing drug release. This study comprises development and characterization of a pyramidal model of dissolving MNs (500 µm) prepared with 5% w/w aminolevulinic acid and 20% w/w Gantrez AN-139 in aqueous blend. Protoporphyrin IX formation and distribution were evaluated in tumor mice model by using fluorescence widefield imaging, spectroscopy, and confocal microscopy. MNs demonstrated excellent mechanical resistance penetrating about 250 µm with minor size alteration *in vitro*, and fluorescence intensity was 5-times higher at 0.5 mm on average compared to cream *in vivo* (being 10±5 a.u. for MNs and 2.4±0.8 a.u. for cream). Dissolving MNs have overcome topical cream application, being extremely promising especially for thicker skin lesions treatment using PDT.

KEYWORDS
Dissolving Microneedles, Aminolevulinic Acid, Protoporphyrin IX, Photodynamic Therapy, Intradermal.

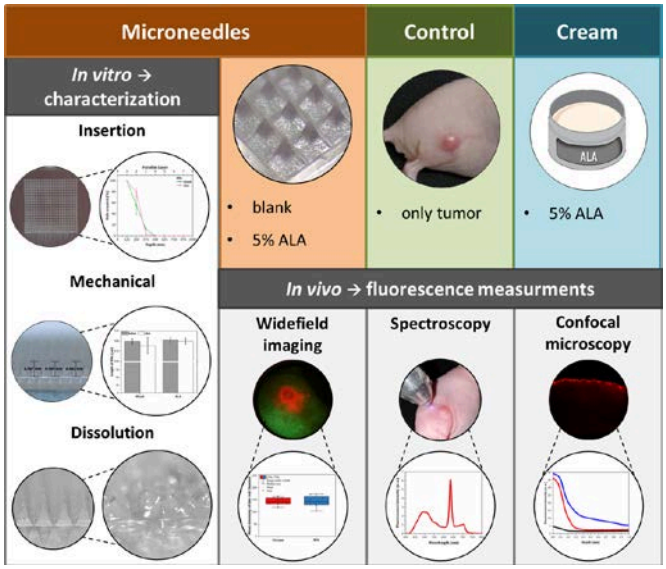

1 | INTRODUCTION

Non-melanoma skin cancer (NMSC) is one of the most frequent cancers. According to the International Agency for Research on Cancer (IARC), about 1 million new lesions occurred in 2018 worldwide [1]. Basal cell carcinoma (BCC) is the most common type of NMSC which usually affects caucasian people and it is mostly found on areas of the body

This article has been accepted for publication and undergone full peer review but has not been through the copyediting, typesetting, pagination and proofreading process which may lead to differences between this version and the Version of Record. Please cite this article as doi: 10.1002/jbio.202000128

exposed to the sun [2]. Even though BCC commonly is a not life-threatening tumor, is slow-growing, and rarely causes metastasis [3], it can causes comorbidity to the patients besides compromising anatomic regions.

Clinically, BCC is a lesion that can be classified as pigmented or non-pigmented and divided into histopathologic subtypes, such as nodular BCC, superficial BCC, morpheaform BCC and infiltrative BCC [4]. Currently, the standard treatment for BCC is still surgery. However, there are non-surgical procedures that have also been applied, such as physical removal methods (curettage, cryosurgery, or electrodesiccation), topical drugs (e.g., 5-fluorouracil, imiquimod, or ingenol mebutate), radiotherapy, hedgehog pathway inhibitors or photodynamic therapy (PDT). The method chosen is normally related to the experience of the physician, depends on the tumor size and location, histopathological subtype, whether they are recurrent tumors, also considering the patient preference, potential adverse events, and cosmetic outcome [5].

Topical PDT has been widely applied both for NMSC and premalignant lesions [6–14]. The main advantages are an ambulatory procedure that in patients with comorbidities, promotes excellent clearance rate and cosmetic results with minimum adverse effects, also allows performance of multiple sessions without causing tumor resistance and preserving the normal tissue [15]. The main photosensitizer (PS) used in topical PDT is the endogenous protoporphyrin IX (PpIX), which is accumulated by the topical application of a cream containing one of its precursors, such as aminolevulinic acid (ALA) or methyl aminolevulinate (MAL) [16]. In terms of these precursors' delivery, there is an important difficulty in administering consistent dosing of cream to standardize protocols and the inadequate release due to the poor drug permeation into the skin layers [17]. Limitations for topical PDT mostly come from light and drug delivery. Assuming light delivery can be handled, alternatives that enable more efficient PpIX precursor delivery may favor the treatment, mainly for nodular lesions which usually have lower PDT response compared to superficial lesions [18].

The enhancement of PpIX precursor penetration into the skin or tumor can be achieved by physical and chemical methods [19]. In terms of physical approaches as pre-treatment, intradermal delivery has been evaluated by the association of microneedles (MNs) rollers [20–23], high-pressure needle-free injections [24–26], iontophoresis [27–30], laser [31,32], and, ultrasound [33,34]. Requena et al. performed experimental and clinical studies using a micropigmentation machine (dermograph) and confirmed that the precursor and consequent formation of PpIX in-depth were more efficient with the intradermal delivery compared to the cream applied topically [35]. Mu et al. applied successfully plum-blossom needles associated with pulsed CO_2 laser to enhance the PDT effect in patients with BCC [36]. However, solid needles are made by a metal matrix which implies using a cream association to deliver the formulation. These solid needles also produce hazardous clinical waste.

Donnelly et al. [37] developed a water-soluble bioadhesive patch formulation containing ALA. To improve the penetration of this compound, MNs have been developed. The MNs are a minimally invasive drug delivery system painlessly and without causing bleeding when inserted into the skin penetrating the stratum corneum [38]. With respect to the ability of this approach in PDT, the administration of silicon MNs puncturing the skin was able to significantly enhance ALA penetration released from bioadhesive patches [39]. Importantly, similar approaches have been applied, including blank dissolving MNs and hydrogel-forming MNs to evaluate the delivery of ALA, methylene blue, and meso-tetra (N-methyl-4-pyridyl) porphine tetra tosylate from bioadhesive path type drug reservoirs [40–42]. However, to the best of our knowledge, ALA has not yet been developed into MNs formulation. Leading on from these promising results, the incorporation of ALA into MNs could be an innovative approach that enables direct administration of this compound to the tumor lesions.

In this study, we propose a dissolving MNs formulation containing ALA. Several ALA concentrations were attempted to optimize the formulations. Afterward, the mechanical and insertion properties were investigated using a standardized method. Finally, to evaluate the efficacy of this novel approach, the efficiency of the intradermal administration of ALA-MNs was carried out in a skin tumor model in mice, compared with the topical application of the cream. The outcomes of this study could potentially open new alternative therapies for BCC.

2 | EXPERIMENTAL

2.1 | Chemicals and materials

ALA in hydrochloride form and cream with 5% w/w ALA were acquired from PDT Pharma (Cravinhos, São Paulo, Brazil). The cream components were previously established and applied in clinical trials [43–45]. The polymer used was the Gantrez® AN-139, a copolymer of methyl vinyl ether and maleic anhydride (PMVE/MAH) (Ashland, Kidderminster, UK). Tissue-Tek® Optimal Cutting-Temperature media was acquired from Sakura Finetek (Torrance, Canada).

2.2 | Preparation of MNs

The dissolving MNs were prepared from aqueous blends containing ALA at 5, 10, and 20% w/w concentration. Gantrez® AN-139 was used as 20% w/w aqueous blends, prepared as previously described [46,47]. ALA was dissolved in the polymer gel. After homogenization in the centrifuge (Eppendorf Centrifuge 5804, Eppendorf, Hamburg, Germany) for 15 minutes at 3500 rpm, the formulation was poured into the silicone molds. Each mold was composed of a dense pyramidal array with 19 x 19 pyramidal holes with arrays ranging about 6.6 x 6.6 mm. The pyramids were 500 µm long and 300 µm wide at the base each, spaced by 50 µm gaps. Blank MNs were prepared using only Gantrez® AN-139 at 20% w/w concentration. The mold with the formulation was placed in a gallon pressure tank (Airprowu®, Airpro Industry Corp., New Taipei, Taiwan) for 5 minutes at 4 bar pressure. This pressurization process was repeated twice. The samples were dried for 48 hours at room temperature. After removal from the molds, the MNs were kept sealed in aluminum pack in the fridge at 5 to 8 ºC.

2.3 Calculation of ALA concentration after dry

The theoretical drug content of the MNs can be calculated based on previous studies [48,49]. Our MNs were prepared from 5% w/w of ALA and 20% w/w of polymer. Therefore, the water content of our formulation was 75% w/w. In the MNs preparation, each MNs array contained about 100 mg (containing approximately 5 mg of ALA) of the formulation in the mold. After drying, we determined the water loss by weighing the dry MNs obtained. The average mass of dry formulation was around 30 mg. Assuming that the mass of ALA was 5 mg, the concentration of ALA in the final formulation was found to be around 17% (5/30 x 100%).

2.4 | Insertion ability, mechanical properties and dissolution time of MNs

The Texture Analyzer System (Stable Micro Systems, Surrey, UK) was used to compress the MNs with a force of 32 N for 30 seconds [50]. The membrane model proposed by Larrañeta *et al.* was explored [51] where the MNs were pressed into a commercial polymeric film (Parafilm® M) folded to get an eight-layer film (Figure 2a). The percentage of holes created in each layer was also estimated following Larrañeta et al. study which the images of the layers were collected by light microscopy (Leica EZ4D, Leica Microsystems, Milton Keynes, UK) and the number the holes counted, considering 361 holes as maximum [51]. An *in vitro* test using excised skin from stillborn piglets was performed with full-thickness skin samples obtained less than 24 hours post-mortem. The samples were kept in sealed Petri dishes at -20 °C. Before the experiments, the hair was removed by a disposable razor and the skin was equilibrated for 30 minutes in phosphate-buffered saline (PBS) at pH 7.4. An optical coherence tomography (OCT) microscope (Michelson Diagnostics Ltd., Kent, UK) was used to evaluate the insertion of the MNs in both models according to the previous studies [48,52]. The image processing software ImageJ® (National Institutes of Health, Bethesda, USA) was used to determine the length of MNs inserted. To evaluate the mechanical properties of the MNs, five random measurements of the MNs lengths in each side of the array were considered to estimate the mean length before and after the compression. The measurements were performed using the light microscopy considering the MNs pressed in the Parafilm® M. To investigate the dissolution of the MNs, the MNs were inserted into the skin section using manual pressure [52,53]. A cylindrical stainless steel mass of 5.0 g was placed on top to assure the array remained in place. MNs were removed at defined time points and directly observed under the microscope. The experiment was carried out at room temperature.

2.5 | Murine tumor model

This study had approval from the Animal Use Ethics Committee of the Sao Carlos Institute of Physics at the

University of Sao Paulo (protocol number 9599080918). A total of 36 female balb/c athymic nude mice were used. The animals were kept with water and food (regular rodent chow) *ad libitum*. During the experiments, the animals were maintained acclimatized ambient at 25 ºC and under inhalation anesthesia. The xenographic tumor induction was performed with a squamous cell carcinoma (SCC) of the human cell line A431, ATCC® CRL-1555™ (Manassas, Virginia, USA). Although being an SCC cell line, these cells provide a model for obtaining a nodular, non-cystic non-melanoma skin cancer which is already well established in the literature, in contrast to BCC induced tumor models [54,55]. For tumor model induction, the inoculation was performed once in the animals' right flanks using intradermal injection (50 µL of suspended cells in PBS at 10^6 cells concentration). Growth monitoring was standardized as a function of the volume in order to perform the experiments on tumors with similar characteristics. A sphere volume was estimated for each tumor with measurements using a vernier caliper. The average radius was obtained from two diameter measurements collected on the surface and a third one considering the diameter in depth.

2.6 | *In vivo* experiment

An *in vivo* pilot study was performed to evaluate the dissolution of the MNs. For two animals, the MNs were applied with 1-hour incubation and for the other two, after the MNs insertion, superficial heating at 40 °C was performed during the first 15 minutes of the 1-hour incubation using a skin heating commercial device (Derme Cool, Dermius, Sao Paulo, Brazil). Based on the results from the pilot study, the heating protocol was used for MNs application only. The confocal fluorescence microscopy assessments were performed with 16 mice (control, cream, ALA-MN, and blank MN), for which the tumor biopsies were snap-frozen in optimal cutting-temperature compound, kept at -80 °C and sectioned at 30 µm using a cryostat (Leica Biosystems, CM1850, UK). Fluorescence widefield images and fluorescence spectroscopy measurements were collected for all animals prior to euthanasia. Table 1 summarizes the mice distribution used in the study according to the protocols evaluated.

TABLE 1: Protocol description and number of mice used; the letters correspond to the fluorescence techniques: W=widefield images, S=spectroscopy, and C=confocal microscopy.

PROTOCOL			MICE			
PILOT						
MN	no heating		2			
	40º C for 15 min		2			
GROUPS				**W**	**S**	**C**
Control	Only tumor		8	8	8	4
Cream	ALA		8	8	8	4
MN	40º C for 15 min	Blank	8	8	8	4
		ALA	8	8	8	4
		TOTAL	**36**			

2.6.1 | Fluorescence widefield imaging

A widefield fluorescence imaging system was used to monitor the superficial PpIX distribution. The system for image acquisition was composed of a LED-based device (λ=400-450 nm, LINCE®, MM Optics, São Carlos, Brazil) coupled to a digital color camera (Sony DSC H50, Sony Corporation of America, New York, USA) [56]. In our experiments, the images were registered by a digital color camera which uses a Bayer filter in front of its sensor. The Bayer filter allows the acquisition of an RGB image in 'jpeg' extension, which means that the camera memory stores three arrays of image data, each containing the information of one specific color (red, green, or blue). The pixel depth for our device is 8 bits, which means that we can describe a pixel in 28 different values (256) for each color, since three arrays are recorded (red, green, and blue), each with a pixel depth of 8 bits, we can have $(28)^3$ different colors for each pixel (more than 16 million colors). When we worked with the red channel, we used only the red array of data, this is why the used that terminology. The fluorescence widefield images were processed using an algorithm developed on Python (Python Software Foundation) using open-source libraries (OpenCV and NumPy) considering the mean intensity of pixels from the RGB red component after splitting the RGB image. This definition was made based on the previous study by Andrade et al., in which the red component has been used as referring to the red fluorescence of PpIX [57]. The region of interest (ROI) was defined manually in the endogenous

fluorescence image for each animal. The algorithm automatically positioned images before and after incubation for each animal based on its ROI for quantification.

2.6.2 | Fluorescence spectroscopy

Fluorescence spectra were collected in animal tests using a system assembled with a spectrophotometer (USB2000, OceanOptics Inc., Dunedin, FL, USA) coupled to a laptop and a diode laser for excitation at 408 nm. A "Y-type" optical fiber was used in order to simultaneously deliver excitation light onto the tumor and collect fluorescence from the tumor surface to be delivered to the spectrometer after passing by a high-pass filter. The optical fiber probe was gently positioned perpendicularly to the tumor surface and five spectra per animal were collected at random spots. The data obtained from the normalized spectra were presented as boxplots using the software Origin® (OriginLab Corporation, Northampton, Massachusetts, USA).

2.6.3 | Confocal fluorescence microscopy

The slides from frozen sections were evaluated by a confocal fluorescence microscope (Zeiss - LSM780, Jena, Germany) using a diode laser (405 nm) for excitation and the fluorescence signal collected in the red channel (630-670 nm). Data processing was based on an algorithm developed in the Python platform. The analysis considered the mean intensity fluorescence emission associated with the PpIX distribution as a function of depth (Figure 8a). Figure 8b shows a false-color image (colormap range from 0 to 75) for easy viewing and manual delimitation of the tumor. The statistical analysis performed for the confocal fluorescence microscopy data was One-Way ANOVA (Tukey test).
Autofluorescence confocal images of MNs arrays were collected (at 408-694 nm) in different focal planes and positions (3D images) to observe the dissolution pattern of MNs, using a laser (800nm) for excitation.

3 | RESULTS AND DISCUSSION

The MNs were produced with different concentrations of ALA. Using 20% w/w concentration in casting blends, it was not possible to remove the MNs from the mold, even after ten days of drying. After four days, the arrays could be removed when we used 10% w/w concentration. However, they were flexible and soft. With 5% w/w concentration of ALA in the casting blends was possible to produce strong MNs after two days of drying.
The stability of the ALA molecule in aqueous solution is described as sensitive to pH, concentration, temperature, and oxygenation [58]. The pH value of the aqueous blend of 20% w/w Gantrez AN-139 was measured as approximately 1.85. Novo et al. reported that ALA at 0.3 M in distilled water (about 3.9% w/w) is stable at pH 2 under many storage conditions [59]. Therefore, the higher concentrations (10 and 20% w/w) of ALA tested in this formulation are probably plasticizing the matrix, making the MNs soft. The ALA may also be hygroscopic, absorbing water from the air, softening the MNs. Therefore, MNs containing 5% ALA were selected for this study. The water reduction obtained was about 70% and the final concentration of the MNs formulation was estimated at 17%. Figure 1 presents the appearance of the MNs by scanning electron microscopy and digital microscopy.

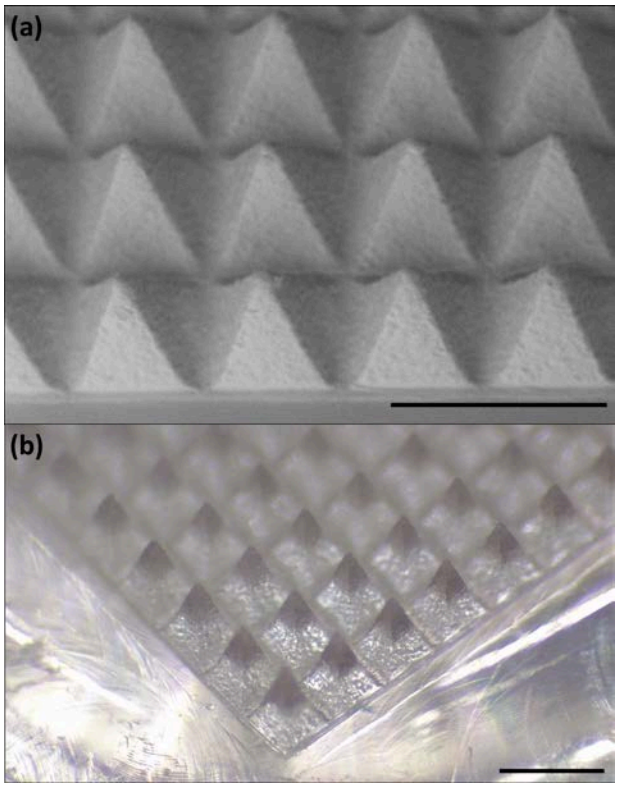

FIGURE 1 MNs prepared from an aqueous blend containing 5% w/w ALA and 20% w/w Gantrez AN-139 concentration: (a) representative scanning electron micrographs of the MNs and (b) illustrative digital image of the array. The scale bars represent 500 µm.

Representative images of the Parafilm M® layers with the holes produced by the ALA-MNs after their insertion are in Figure 2. The percentage of holes created comparing blank MNs and ALA-MNs are presented in Figure 2f. The response of the MNs with ALA was better compared to the blank MNs, where about 80% of ALA-MNs have penetrated up to 250 µm depth and about 55% of the blank MNs achieved the same depth.

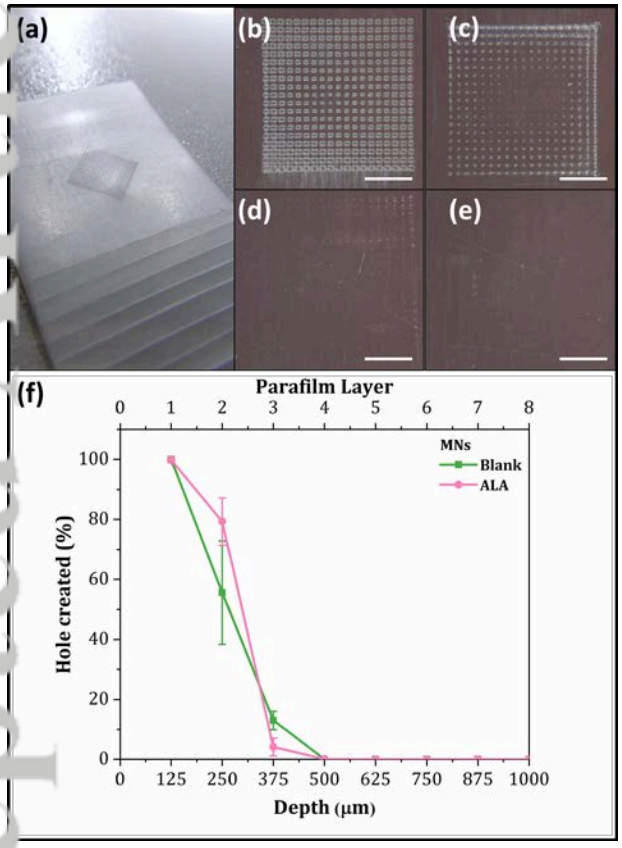

FIGURE 2 (a) Parafilm M® layers mounted for the insertion test. Representative microscopy images of each perforated Parafilm M® layer after insertion of the MNs array showing (b) first, (c) second, (d) third, and (e) fourth layers. The scale bars represent 2 mm. (f) Percentage of holes created for blank and ALA-MNs considering each layer and applying 32 N for 30 seconds. The MNs are approximately 500 µm long each and the array has 19×19 MNs. The data and the error bars represented the means ± SD, n=4 MNs.

In the microscope, the MNs length was measured before and after compression and these results are presented in Figure 3. The blank MNs presented about 2% deformation compared with 0.5% of the ALA-MNs.

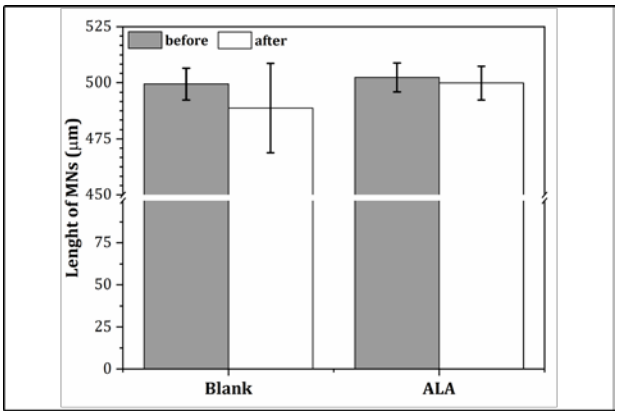

FIGURE 3 MNs length before and after compression for formulations only 20% Gantrez AN-139 (blank) and 20% Gantrez AN-139 with 5% ALA (ALA). The data and the error bars represented the means ± SD, n=4 MNs.

According to the insertion and compression tests, the MNs prepared from aqueous blends containing ALA at 5% w/w concentration presented excellent mechanics resistance with a negligible length decrease, besides about 80% of the MNs with up to 250 µm penetration depth. Oltulu et al. [60] considered different human body regions to estimate the mean epidermis thickness by a histometric technique and reported the intervals of 76.9 to 267.4 µm for women and 112.4 to 244.8 µm for men. Such a comparison shows there is potential for ALA-MNs to be able to perform intradermal delivery in human skin.

The penetration properties and dissolution time of MNs were also observed using OCT. This technique has been successfully applied to evaluate the penetration depth of MNs [48,61]. Figure 4 shows the penetration depth of MNs into Parafilm® M and full-thickness neonatal porcine skin observed using OCT.

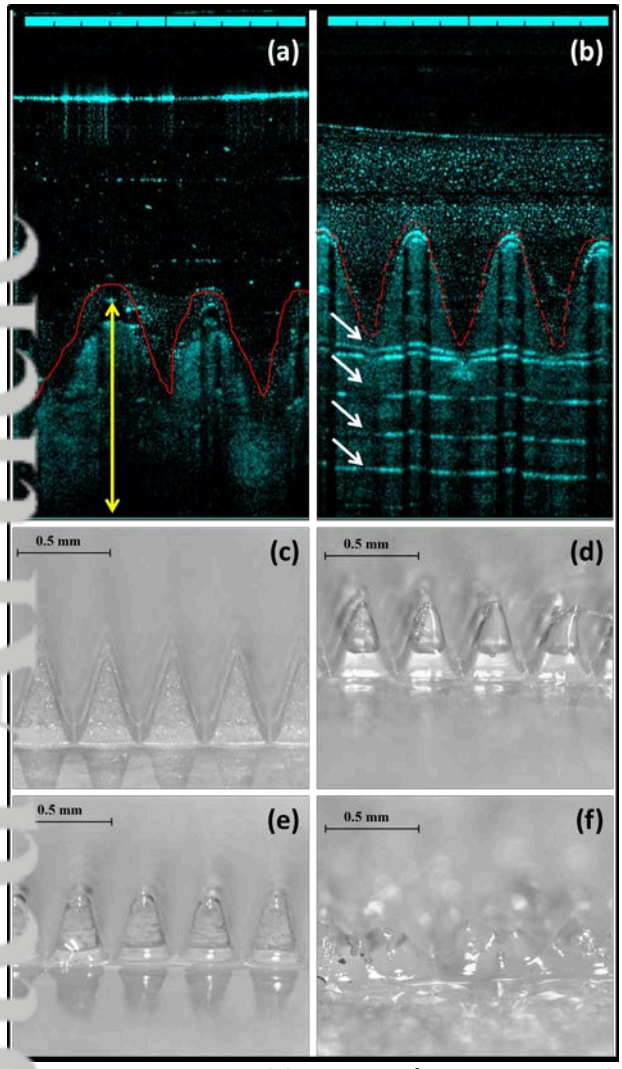

FIGURE 4 Representative OCT images of MNs containing ALA following insertion into (a) full-thickness neonatal porcine skin and (b) Parafilm® M layers (blue scale bar represents a length of 1 mm). The traced lines (in red) show the interface of the MNs array with the skin (indicated by the yellow arrow) or the Parafilm® M layers (indicated by the white arrows). Illustrative digital micrographs of the dissolution of MNs formulations containing ALA at (c) 0 (d) 5, (e) 10 and, (f) 20 minutes, following insertion into, and removal from, excised full-thickness neonatal porcine skin (scale bars represent 0.5 mm).

The results revealed that the 380 ± 10 µm and 370 ± 20 µm of the MNs length when inserted into Parafilm® M and full-thickness neonatal porcine skin, respectively. Figure 4f shows that the MNs completely dissolved in the full-thickness neonatal porcine skin after 20 minutes.

The mean tumor volume in the experiments was about 26 ± 2 mm³. In a pilot study to evaluate the MNs dissolution in the tumor model, the MNs had not presented significant length reduction 1 hour after insertion. Therefore, the superficial heating protocol was applied to stimulate dissolution after the MNs insertion.

Figure 5 shows representative images of the endogenous fluorescence of the tumor and the fluorescence 1 hour after incubation. For all the animals, the values of intensity for the red channel before incubation were negligible compared to the values observed after incubation. The blank MNs did not present red fluorescence (related to the PpIX) in the tumor after incubation, as expected. The mean intensity in the red channel of the fluorescence widefield images had not presented a significant difference between the ALA protocols (Figure 5c).

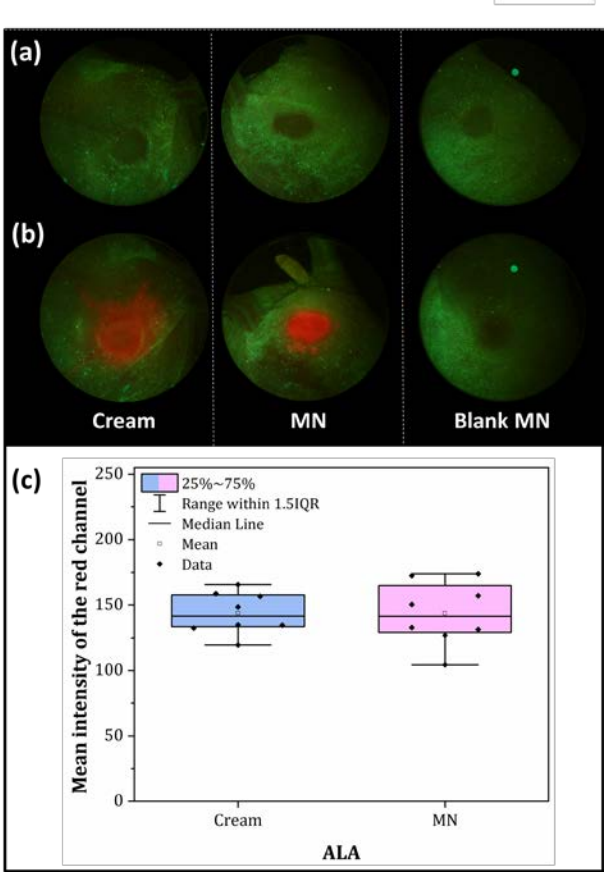

FIGURE 5 (a) Representative widefield fluorescence images collected before cream or MNS application, (b) endogenous

autofluorescence of tumor and surrounding skin and (c) 1 hour after incubation for ALA cream, dissolving MNs containing ALA and blank MNs (only polymer). (d) Boxplot graph displaying the values of the mean intensity of the red channel in the tumor 1 hour after ALA-incubation via cream or MNS. Each symbol '♦' represents the mean intensity value estimated for the image collected for each animal (n = 8 mice).

Figure 6 shows representative images of the MNs array after dissolution in the *in vivo* experiment collected in the confocal fluorescence microscopy. These images were obtained in order to observe the dissolution of MNs through the array. Figure 2 and Figure 6 show visually similar patterns, although different information is presented. MNs arrays are not perfectly flat, but the texture analyzer probe is, thus producing different pressure onto the array when performing the *in vitro* perforation test. This unevenness is irrelevant for *in vivo* perforation since pressure is manually applied, ensuring more homogeneous pressure onto the arrays. For Figure 6 the pattern is related to the uneven dissolution within the array. On the edges of the array, dissolution is not observed and whole MNs can be found after application since these MNs do not reach the skin tissue around the tumor.

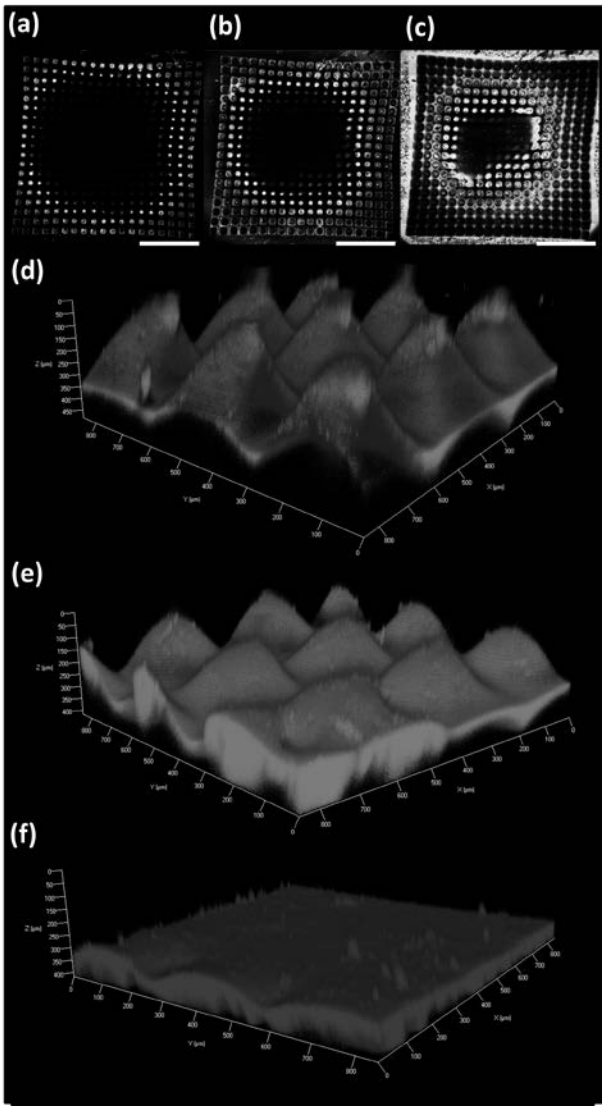

FIGURE 6 Representative confocal fluorescence microscopy image of the MNs array after remaining inserted for 1 hour onto the tumor for dissolution when associated with the heating protocol *in vivo*. Image collected in a (a) more superficial, (b) intermediate, and (c) deep planes of the array. The scale bar represents 2 mm. 3D images from the MNs were collected in the (d) edge, (e) middle and, (f) center of the array observed in the image (c).

The maximum emission of endogenous fluorescence of the skin and the tumor is located around 500 nm (Figure 7a) [62]. The 450 nm wavelength presents minimum fluorescence intensity variation [62] and it was chosen for the normalization of each spectrum. The fluorescence emission at 635 nm is associated with PpIX concentration [63]. Therefore,

the values of the normalized fluorescence intensity at this wavelength were used to compare the PpIX accumulation after cream or MNs incubation (Figure 7b). An increase of 200% in the mean fluorescence intensity was observed for the ALA-MNs compared to the ALA cream protocol.

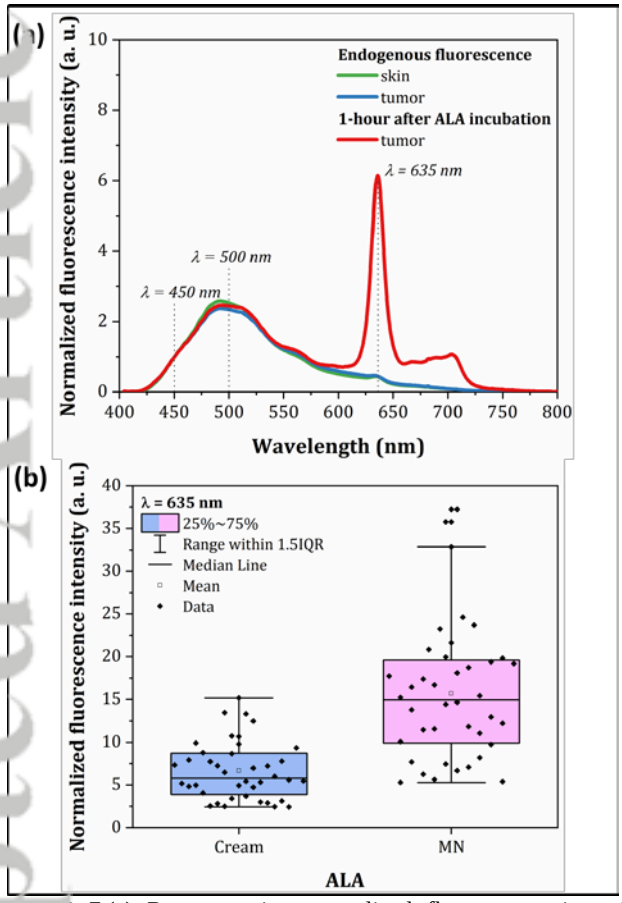

FIGURE 7 (a) Representative normalized fluorescence intensity spectra of tumor and skin endogenous autofluorescence and 1 hour after ALA incubation in the tumor. (d) Boxplot graph displaying normalized fluorescence intensity values in the tumor 1 hour after ALA-incubation *via* cream or MNs. For each animal (n = 8 mice), 5 spectra were collected and each symbol '♦' represents the normalized fluorescence intensity value at 635 nm obtained from each spectrum.

Figure 8 represents confocal fluorescence data obtained from frozen tumor sections. Figures 8a, 8b, and 8c describe the image processing steps. Figures 8d, 8e, and 8f are representative images from the red channel for a control tumor, and tumors collected one hour after ALA was applied *via* cream or dissolving MNs, respectively. Figure 8g presents the fluorescence intensity quantification as a function of depth for all conditions. In Figure 8c, the letter 'A' identifies the region of interest demarcated to minimize edge effects (yellow dashed lines), and the letter 'Z' indicates the depth direction of PpIX formation. The algorithm considered 30 areas (delimited by white lines) along the tumor depth to estimate the mean fluorescence intensity in each region.

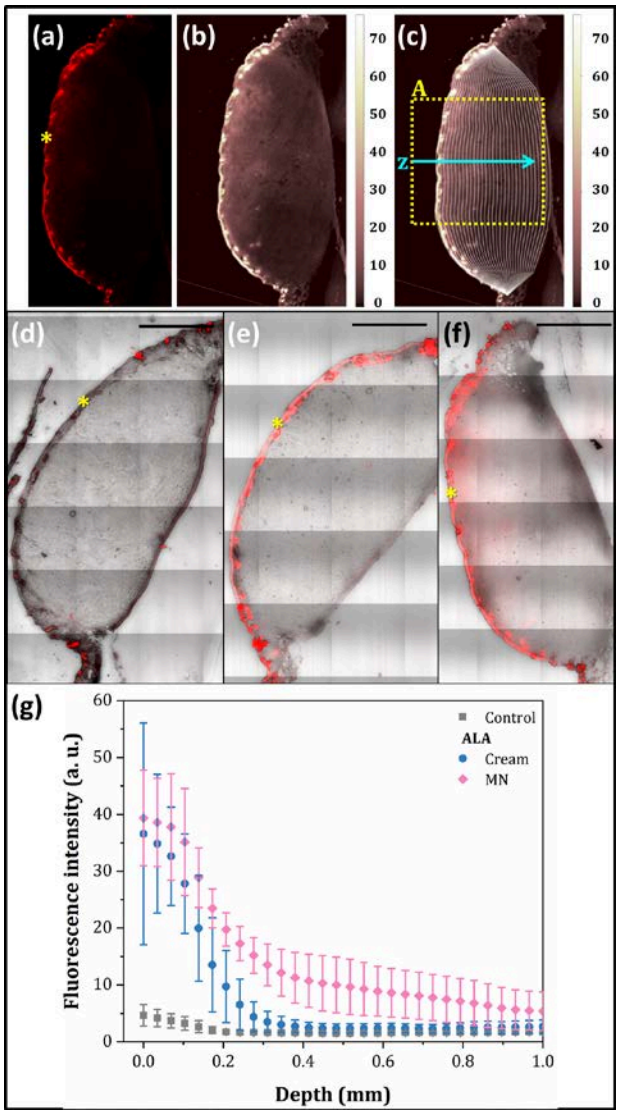

FIGURE 8 Scheme of steps of fluorescence confocal microscopy images processing from frozen tumor sections: (a) the red channel image, (b) a false-color image (colormap range from 0 to 75), (c) the letter 'A' represents the region of interest in the analysis (yellow dashed lines), the letter 'z' indicates the depth direction of PpIX formation considering 30 areas (delimited by white lines) along the

tumor depth. Representative confocal fluorescence microscopy images of the red channel overlapped with transmission image: (d) tumor without sensitization (control), (e) tumor 1 hour after topical cream application, (f) tumor 1 hour after intradermal MNs application. The symbol '*' indicates the epidermis layer. The scale bar represents 1 mm. (g) Fluorescence intensity in the red channel as a function of tumor depth for control, 1 hour after ALA *via* cream or MNs. The data and the error bars represented the means ± SD, n=4 mice, p = 0.05 from One Way ANOVA Tukey post-test.

According to Figure 8e and 8f, it was not possible to observe significant differences in fluorescence intensity on the epidermis layer after ALA incubation which can be associated with its below selectivity. However, by the MNs protocol, there is a greater fluorescence signal in deeper layers of the tumor that means the ALA was delivered at greater depths allowing the higher production and distribution of the PpIX compared to the cream topical application. After image processing, it is possible to observe from Figure 8g that, up to 0.2 mm, no significant difference in fluorescence intensity were observed between ALA applications ($p>0.05$). For depths greater than 0.2 mm, however, the ALA-MNs protocol always presented higher fluorescence intensity compared with ALA cream (about 5 times higher on average at 0.5 mm, being 10 ± 5 a. u. for MNs and 2.4 ± 0.8 a. u. for cream), with a statistically significant difference until approximately 0.8 mm ($p<0.05$).

Through the superficial fluorescence quantification techniques, no significant difference was observed when comparing the cream with the dissolving MNs, either by fluorescence spectroscopy or fluorescence widefield imaging. However, after evaluation of the biopsies collected after 1-hour incubation, it was possible to observe that the depth distribution of the PpIX occurred more efficiently through the application of dissolving MNs with statistically significant difference ($p<0.05$).

The debulking or curettage has been described as an important tool to facilitate cream permeation and improve the PDT response [64,65]. However, these procedures offer some discomfort to the patients in addition to causing bleeding that can also interfere with cream penetration efficiency. Even being adopted today as part of protocols, it is interesting to present alternatives. In this aspect, the dissolving MNs might be an option for improving the precursor's delivery to greater depths without causing any pain.

The pain during the PDT irradiation also is a relevant concern and it is highly related to the patient acceptance for the treatment [66]. MNs prepared from 30% w/w aqueous solution of PMVE/MA were applied in human skin as a pre-treatment before ALA or MAL cream application at 2, 8, and 16% concentrations and non-significant increase of erythema or pain during PDT irradiation were observed. An increase of the PpIX fluorescence was reported after 4 hours incubation with 2% and 8% w/w ALA or MAL cream also using MNs as a pre-treatment [67].

The cream formulation containing 20% or 16% (w/w) of PpIX precursors has attracted widespread use. However, the problem related to the amount of cream applied and the ensuing cutaneous dose, the occlusion adds to this problem, giving a non-uniform distribution of cream which inevitably makes the comparison of results from clinical studies difficult [37]. The MNs presented greater potential in deeper PpIX distribution compared to the cream both prepared with 5% w/w concentration. More tests using the cream with ALA at 20% w/w concentration still need to be performed to compare the efficiency of the dissolving ALA-MNs. Based on our clinical experience, about 300 mg of the cream containing 20% w/w PpIX precursor is used to perform two sessions of PDT for a BCC lesion treatment. [68]. In this context, the dissolving MNs besides providing a more standardized delivery may contribute to PDT dissemination due to potential cost improvements by a lower drug concentration needed.

There are many benefits and challenges of translating the MNs as drug delivery systems into clinical practice. However, MNs have been widely studied and had demonstrated flexibility in the application in treating several dermatological conditions [69].

4 | CONCLUSION

Our results demonstrated that the dissolving MNs have overcome topical cream application in PpIX distribution, suggesting that this intradermal delivery approach is extremely promising, especially for the treatment of thicker skin lesions using PDT. Following these promising results, the next step should now be carried out regarding the effectiveness of this approach in clinical studies.

ACKNOWLEDGMENTS

We acknowledge support from PDT Pharma Company, the Brazilian Development Bank (BNDES) [grant numbers 09.2.1458.1], São Paulo Research Foundation (FAPESP) [grant numbers 2013/07276-1 (CEPOF), 2009/54035-4 (EMU), 2014/50857-8 (INCT)] and the internship support from Coordination for the Improvement of Higher Education Personnel (CAPES) [grant numbers 88881.132995/2016-01]. This study was also supported in part by Welcome Trust [grant numbers WT094085MA]. In addition, we thank Patrick Oliveira Feitosa (University of São Paulo) for providing computational assistance.

CONFLICT OF INTEREST

The authors declare no financial or commercial conflict of interest.

REFERENCES

[1] J. Ferlay, Estimating the global cancer incidence and mortality in 2018 : GLOBOCAN sources and methods, *Int. J. Cancer*. **2019**, 144, 1941. doi:10.1002/ijc.31937.

[2] M. Zak-Prelich, J. Narbutt, A. Sysa-Jedrzejowska, Environmental Risk Factors Predisposing to the Development of Basal Cell Carcinoma, Dermatologic Surg. **2004**, 30, 248. doi:10.1111/j.1524-4725.2004.30089.x.

[3] P. T. Ting, R. Kasper, J. P. Arlette, Metastatic basal cell carcinoma: Report of two cases and literature review, *J. Cutan. Med. Surg*. **2005**, 9, 10. doi:10.1007/s10227-005-0027-1.

[4] M. Ofer Reiter, I. Mimouni, S. Dusza et al., Dermoscopic Features of Basal Cell Carcinoma and its Subtypes: A systematic Review, *J. Am. Acad. Dermatol*. **2019**. doi:doi.org/10.1016/j.jaad.2019.11.008.

[5] J. Paoli, J. Dahlén Gyllencreutz, J. Fougelberg et al., Nonsurgical Options for the Treatment of Basal Cell Carcinoma, *Dermatol. Pract. Concept.* **2019**, 9, 75. doi:10.5826/dpc.0902a01.

[6] Z. Tehranchinia, H. Rahimi, M.S.M.S. Ahadi et al., Aminolevulinic Acid-photodynamic therapy of Basal cell carcinoma and factors affecting the response to treatment: a clinical trial., *Indian J. Dermatol*. **2013**, 58, 327. doi:10.4103/0019-5154.113968.

[7] M. B. Ericson, A. M. Wennberg, O. Larkö, Review of photodynamic therapy in actinic keratosis and basal cell carcinoma., *Ther. Clin. Risk Manag.* **2008**, 4, 1.

[8] M. Cai, P. Fu, D. Q. Deng et al., Efficacy of ALA-PDT in the treatment of fifty cases of skin cancers and precancerous dermatosis, *J. Clin. Dermatology*. **2009**, 38, 605.

[9] C. Matei, M. Tampa, T. Poteca et al., Photodynamic therapy in the treatment of basal cell carcinoma, *J. Med. Life*. **2013**, 6, 50. http://www.ncbi.nlm.nih.gov/pubmed/23599819.

[10] M. T. Wan, J. Y. Lin, Current evidence and applications of photodynamic therapy in dermatology, *Clin. Cosmet. Investig. Dermatol.* **2014**, 2014, 145. doi:10.2147/CCID.S35334.

[11] C. a Morton, C. Whitehurst, J. H. McColl et al., Photodynamic therapy for large or multiple patches of Bowen disease and basal cell carcinoma., *Arch. Dermatol*. **2001**, 137, 319.

[12] J. A. Suarez-Perez, E. Herrera, E. Herrera-Acosta et al., Photodynamic therapy in the treatment of extensive Bowen disease, *J. Am. Acad. Dermatol*. **2013**, 68, 164.

[13] J. Han, J. E. Kim, G. H. Park et al., Photodynamic therapy of the Bowen disease, *J. Dermatol*. **2012**, 39, 252.

[14] R. M. Szeimies, P. Radny, M. Sebastian et al., Photodynamic therapy with BF-200 ALA for the treatment of actinic keratosis: results of a prospective, randomized, double-blind, placebo-controlled phase III study., *Br. J. Dermatol*. **2010**, 163, 386. doi:10.1111/j.1365-2133.2010.09873.x.

[15] K. Nguyen, A. Khachemoune, An update on topical photodynamic therapy for clinical dermatologists, *J. Dermatolog. Treat*. **2019**, 30, 732. doi:10.1080/09546634.2019.1569752.

[16] L. Griffin, J. Lear, Photodynamic Therapy and Non-Melanoma Skin Cancer, *Cancers (Basel)*. **2016**, 8, 98. doi:10.3390/cancers8100098.

[17] D. I. J. Morrow, M. J. Garland, P. A. McCarron et al., Innovative drug delivery strategies for topical photodynamic therapy using porphyrin precursors, *J. Environ. Pathol. Toxicol. Oncol*., **2007**, 26. doi:10.1615/JEnvironPatholToxicolOncol.v26.i2.50.

[18] M. Fernández-Guarino, A. Harto, B. Pérez-García et al., Six Years of Experience in Photodynamic Therapy for Basal Cell Carcinoma: Results and Fluorescence Diagnosis from 191 Lesions, *J. Skin Cancer*. **2014**, 2014, id: 849248. doi:10.1155/2014/849248.

[19] L. W. Zhang, Y. P. Fang, J. Y. Fang, Enhancement techniques for improving 5-aminolevulinic acid delivery through the skin, *Dermatologica Sin*. **2011**, 29, 1. doi:10.1016/j.dsi.2011.02.002.

[20] P. G. S. Rodrigues, P. F. C. de Menezes, A. K. L. Fujita et al., Assessment of ALA-induced PpIX production in porcine skin pretreated with microneedles, *J. Biophotonics*. **2015**, 8, 723. doi:10.1002/jbio.201400081.

[21] J. M. Spencer, S. A. Freeman, Microneedling prior to Levulan PDT for the treatment of actinic keratoses: A split-face, blinded trial, *J. Drugs Dermatology*. **2016**, 15, 1072.

[22] L. Torezan, Y. Chaves, A. Niwa et al., A pilot split-face study comparing conventional methyl aminolevulinate- photodynamic therapy (PDT) with microneedling-assisted PDT on actinically damaged skin, *Dermatologic Surg*. **2013**, 39, 1197. doi:10.1111/dsu.12233.

[23] T. A. Petukhova, L. A. Hassoun, N. Foolad et al., Effect of expedited microneedle-assisted photodynamic therapy for field treatment of actinic keratoses: A randomized clinical trial, *JAMA Dermatology*. **2017**, 153, 637. doi:10.1001/jamadermatol.2017.0849.

[24] Y. Gong , S. Labh, Y. Jin et al., Needle-free injection of 5-aminolevulinic acid in photodynamic therapy for the treatment of non-melanoma skin cancer, *Dermatol. Ther*. **2016**, 29, 255. doi:10.1111/12335.

[25] P. G. S. Rodrigues, P. F. C. de Menezes, M. B. Requena, et al., New alternatives to improve the transdermal application of ALA, M-ALA in photodynamic therapy using needle-free injection, *Photodiagnosis Photodyn. Ther*. **2015**, 12, 360. doi:10.1016/j.pdpdt.2015.07.138.

[26] D. Barolet, A. Boucher, No-needle jet intradermal aminolevulinic Acid photodynamic therapy for recurrent nodular Basal cell carcinoma of the nose: a case report., *J. Skin Cancer*. **2011**, 2011, id: 790509. doi:10.1155/2011/790509.

[27] H. Osman-Ponchet, A. Gaborit, K. Sevin et al., Pretreatment of skin using an abrasive skin preparation pad, a microneedling device or iontophoresis improves absorption of methyl aminolevulinate in ex vivo human skin, *Photodiagnosis Photodyn. Ther*. **2017**, 20, 130. doi:10.1016/j.pdpdt.2017.09.006.

[28] H. E. Boddé, P. E. H. Roemelé, W. M. Star et al., Quantification of Topically Delivered 5-Aminolevulinic Acid by Iontophoresis Across Ex Vivo Human Stratum Corneum¶, *Photochem. Photobiol*. **2002**, 75, 418. doi:10.1562/0031-8655(2002)0750418qotdaa2.0.co2.

[29] K. Mizutani, D. Watanabe, Y. Akita et al., Photodynamic therapy using direct-current pulsed iontophoresis for 5-aminolevulinic acid application, *Photodermatol. Photoimmunol. Photomed*. **2009**, 25, 280. doi:10.1111/j.1600-0781.2009.00456.x.

[30] C. N. Lemos, J. G. De Souza, P. S. Simão et al., Iontophoresis improved growth reduction of invasive squamous cell carcinoma in topical photodynamic therapy, *PLoS One*. **2016**, 11, e0145922. doi:10.1371/journal.pone.0145922.

[31] F. Vrani, E. Sotiriou, E. Lazaridou et al., Short incubation fractional CO 2 laser-assisted photodynamic therapy vs. conventional photodynamic therapy in field-cancerized skin: 12-month follow-up results of a randomized intraindividual comparison study, *J. Eur. Acad. Dermatology Venereol*. **2019**, 33, 79. doi:10.1111/jdv.15109.

[32] T. Steeb, J. G. Schlager, C. Koh et al., Laser-assisted photodynamic therapy for actinic keratosis: A systematic review and meta-analysis, *J. Am. Acad. Dermatol*. **2019**, 80, 497, doi:10.1016/j.jaad.2018.09.021.

[33] R. Smucler, M. Kriz, J. Lippert et al., Ultrasound Guided Ablative-Laser Assisted Photodynamic Therapy of Basal Cell Carcinoma (US-aL-PDT), *Photomed. Laser Surg*. **2012**, 30, 200. doi:10.1089/pho.2011.3107.

[34] L. Ma, J. Moan, Q. Peng, et al., Production of protoporphyrin IX induced by 5-aminolevulinic acid in transplanted human colon adenocarcinoma of nude mice can be increased by ultrasound, *Int. J. Cancer*. **1998**, 78, 46. doi:10.1002/(SICI)1097-0215(19981109)78:4<464::AID-IJC12>3.0.CO;2-6.

[35] M. B. Requena, P. E. Russignoli, J. D. Vollet-Filho et al., Use of dermograph for improvement of PpIX precursor's delivery in Photodynamic Therapy: experimental and clinical pilot studies, *Photodiagnosis Photodyn. Ther*. **2019**, 29, 101599. doi:10.1016/j.pdpdt.2019.101599.

[36] X. Mu, L. Wang, L. Wang, et al., Plum-blossom needling enhanced the effect of photodynamic therapy on basal cell carcinoma, *Photodiagnosis Photodyn. Ther*. **2018**, 23, 339. doi:10.1016/j.pdpdt.2018.08.001.

[37] P. A. McCarron, R. F. Donnelly, A. Zawislak et al., Design and evaluation of a water-soluble bioadhesive patch formulation for cutaneous delivery of 5-aminolevulinic acid to superficial neoplastic lesions, *Eur. J. Pharm. Sci*. **2006,** 27, 268. doi:10.1016/j.ejps.2005.10.009.

[38] H. S. Gill, D. D. Denson, B. A. Burris et al., Effect of microneedle design on pain in human volunteers, *Clin. J. Pain*. **2008,** 24, 585. doi:10.1097/AJP.0b013e31816778f9.

[39] R. F. Donnelly, D. I. J. Morrow, P. A. McCarron et al., Microneedle-mediated intradermal delivery of 5-aminolevulinic acid: Potential for enhanced topical photodynamic therapy, *J. Control. Release*. **2008**, 129, 154. doi:10.1016/j.jconrel.2008.05.002.

[40] R. F. Donnelly, D. I. J. Morrow, M. T. C. McCrudden et al., Hydrogel-forming and dissolving microneedles for enhanced delivery of photosensitizers and precursors, *Photochem. Photobiol*., **2014**, 94, 641. doi:10.1111/php.12209.

[41] R. F. Donnelly, D. I. J. Morrow, P.A. McCarron et al., Microneedle arrays permit enhanced intradermal delivery of a preformed photosensitizer, *Photochem. Photobiol*. **2009**, 85, 195. doi:10.1111/j.1751-1097.2008.00417.x.

[42] R. F. Donnelly, C. M. Cassidy, R.G. Loughlin et al., Delivery of Methylene Blue and meso-tetra (N-methyl-4-pyridyl) porphine tetra tosylate from cross-linked poly(vinyl alcohol) hydrogels: A potential means of photodynamic therapy of infected wounds, *J. Photochem. Photobiol. B Biol*. **2009**, 96, 223. doi:10.1016/j.jphotobiol.2009.06.010.

[43] D. P. Ramirez, C. Kurachi, N. M. Inada et al., Experience and BCC subtypes as determinants of MAL-PDT response: Preliminary results of a national Brazilian project, *Photodiagnosis Photodyn. Ther*. **2014**, 11, 22. doi:10.1016/j.pdpdt.2013.11.001.

[44] K. C. Blanco, L. T. Moriyama, N. M. Inada et al., Fluorescence guided PDT for optimization of the outcome of skin cancer

treatment, *Front. Phys*. 3, **2015**. doi:10.3389/fphy.2015.00030.

[45] D. P. Ramirez, L. T. Moriyama, E. R. de Oliveira et al., Single visit PDT for basal cell carcinoma – a new therapeutic protocol, *Photodiagnosis Photodyn. Ther*. **2019**, 26, 375. doi:doi.org/10.1016/j.pdpdt.2019.04.016.

[46] R. F. Donnelly, R. Majithiya, T. R. R. Singh et al., Design, optimization and characterisation of polymeric microneedle arrays prepared by a novel laser-based micromoulding technique, *Pharm. Res*. **2011**, 28, 41. doi:10.1007/s11095-010-0169-8.

[47] T. R. Raj Singh, P. A. McCarron, A. D. Woolfson, et al., Investigation of swelling and network parameters of poly(ethylene glycol)-crosslinked poly(methyl vinyl ether-co-maleic acid) hydrogels, *Eur. Polym. J*. **2009**, 45, 1239. doi:10.1016/j.eurpolymj.2008.12.019.

[48] A. D. Permana, I. A. Tekko, M. T. C. McCrudden et al., Solid lipid nanoparticle-based dissolving microneedles: A promising intradermal lymph targeting drug delivery system with potential for enhanced treatment of lymphatic filariasis, *J. Control. Release*. **2019**, 316, 34. doi:10.1016/j.jconrel.2019.10.004.

[49] M.T.C. Mc Crudden, E. Larrañeta, A. Clark, et al., Design, formulation and evaluation of novel dissolving microarray patches containing a long-acting rilpivirine nanosuspension, *J. Control. Release*. **2018**, 292, 119. doi:10.1016/j.jconrel.2018.11.002.

[50] R. F. Donnelly, K. Moffatt, A. Z. Alkilani et al., Hydrogel-forming microneedle arrays can be effectively inserted in skin by self-application: A pilot study centred on pharmacist intervention and a patient information leaflet, *Pharm. Res*, **2014**, 31, 1989, doi:10.1007/s11095-014-1301-y.

[51] E. Larrañeta, J. Moore, E. M. Vicente-Pérez et al., A proposed model membrane and test method for microneedle insertion studies, *Int. J. Pharm*. **2014**, 472, 65. doi:10.1016/j.ijpharm.2014.05.042.

[52] P. González-Vázquez, E. Larrañeta, M. T. C. McCrudden et al., Transdermal delivery of gentamicin using dissolving microneedle arrays for potential treatment of neonatal sepsis, *J. Control. Release*. **2017**, 265, 30 . doi:10.1016/j.jconrel.2017.07.032.

[53] R.F. Donnelly, M.T.C. McCrudden, A.Z. Alkilani, et al., Hydrogel-forming microneedles prepared from "super swelling" polymers combined with lyophilised wafers for transdermal drug delivery, *PLoS One*. **2014,** 9, e111547. doi:10.1371/journal.pone.0111547.

[54] D. T. Ho, S. Wykoff-Clary, C. S. Gross et al., Growth inhibition of an established A431 xenograft tumor by a full-length anti-EGFR antibody following gene delivery by AAV., *Cancer Gene Ther*. **2009**, 16, 184. doi:10.1038/cgt.2008.68.

[55] M. Di Benedetto, a Starzec, R. Vassy, G. Y. Perret, et al., Inhibition of epidermoid carcinoma A431 cell growth and angiogenesis in nude mice by early and late treatment with a novel dextran derivative., *Br. J. Cancer*. **2003**, 88, 1987. doi:10.1038/sj.bjc.6600985.

[56] C. Grecco, H. H. Buzzá, M. D. Stringasci et al., Single LED-based device to perform widefield fluorescence imaging and photodynamic therapy, *SPIE Proc*., **2015**, 953121:1–10. doi:10.1117/12.2185925.

[57] C. T. Andrade, J. D. Vollet-Filho, A. G. Salvio et al., Identification of skin lesions through aminolaevulinic acid-mediated photodynamic detection., *Photodiagnosis Photodyn. Ther*. **2014**, 11, 409. doi:10.1016/j.pdpdt.2014.05.006.

[58] R. F. Donnelly, P. A. McCarron, D. Woolfson, Derivatives of 5-aminolevulinic Acid for photodynamic therapy, *Perspect. Medicin. Chem*. **2007**, 1, 49.

[59] M. Novo, G. Hüttmann, and H. Diddens, Chemical instability of 5-aminolevulinic acid used in the fluorescence diagnosis of bladder tumours, *J. Photochem. Photobiol. B Biol*. **1996**, 34, 143. doi:10.1016/1011-1344(96)07285-5.

[60] P. Oltulu, B. Ince, N. Kökbudak et al., Measurement of epidermis, dermis, and total skin thicknesses from six different body regions with a new ethical histometric technique, *Turk Plast. Rekonstruktif ve Estet. Cerrahi Derg*. **2018**, 26, 56. doi:10.4103/tjps.tjps_2_17.

[61] R. F. Donnelly, M .J. Garland, D. I. J. Morrow et al Optical coherence tomography is a valuable tool in the study of the effects of microneedle geometry on skin penetration characteristics and in-skin dissolution, *J. Control. Release*. **2010**, 147, 333. doi:10.1016/j.jconrel.2010.08.008.

[62] E. Borisova, P. Pavlova, E. Pavlova et al., Optical biopsy of human skin - A tool for cutaneous tumours' diagnosis, *Int. J. Bioautomation*. **2012**,16, 53.

[63] K. R. Rollakanti, S. C. Kanick, S. C. Davis et al., Techniques for fluorescence detection of protoporphyrin IX in skin cancers associated with photodynamic therapy, *Photonics Lasers Med*. **2013**, 2. doi:10.1515/plm-2013-0030.

[64] A. M. Soler, T. Warloe, A. Berner et al., A follow-up study of recurrence and cosmesis in completely responding superficial and nodular basal cell carcinomas treated with methyl 5-aminolaevulinate-based photodynamic therapy alone and with prior curettage, *Br. J. Dermatol*. **2008**, 145, 467. doi:10.1111/j.1365-2133.2001.04407.x.

[65] M. R.T. M. Thissen, C. A. Schroeter, and, H. A. M. Neumann, Photodynamic therapy with delta-aminolaevulinic acid for nodular basal cell carcinomas using a prior debulking technique, *Br. J. Dermatol*. **2000**, 142, 338. doi:10.1046/j.1365-2133.2000.03404.x.

[66] J. M. Ang, I. Bin Riaz, M. U. Kamalet al., Photodynamic therapy and pain: A systematic review, *Photodiagnosis Photodyn. Ther*. **2017**, 19, 208. doi:10.1016/j.pdpdt.2017.07.002.

[67] P. Mikolajewska, R. F. Donnelly, M. J. Garlan et al., Microneedle pre-treatment of human skin improves 5-aminolevulininc acid (ALA)- and 5-aminolevulinic acid methyl ester (MAL)-induced PpIX production for topical photodynamic therapy without increase in pain or erythema, *Pharm. Res*. **2010**, 27, 2213. doi:10.1007/s11095-010-0227-2.

[68] H. H. Buzzá, L. T. Moriyama, J. D. Vollet-Filho et al.,, Overall Results for a National Program of Photodynamic Therapy for Basal

Cell Carcinoma: A Multicenter Clinical Study to Bring New Techniques to Social Health Care, *Cancer Control*. **2019**, 26. doi:10.1177/1073274819856885.

[69] A. H. Sabri, J. Ogilvie, K. Abdulhamid et al.,, Expanding the applications of microneedles in dermatology, *Eur. J. Pharm. Biopharm.* **2019**, 140, 121. doi:10.1016/j.ejpb.2019.05.001.

Graphical Abstract for Table of Contents

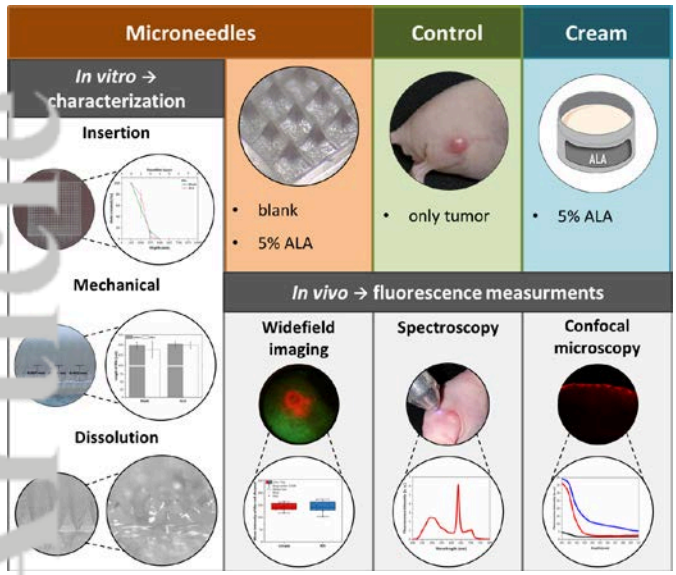

This study showed how dissolving microneedles made with an aqueous blend of aminolevulinic acid and Gantrez AN-139 polymer can improve penetration of protoporphyrin IX into deeper layers of tissue, aimed at skin cancer treatment. Mechanical tests showed microneedles are suitable for the application, and mice skin tumor model tests showed an increase of about was 5-times higher at 0.5 mm on average compared to the cream in vivo (being 10 ± 5 a. u. for MNs and 2.4 ± 0.8 a. u. for cream). in the fluorescence produced by the photosensitizer, evidencing the improvement offered by this approach.